I&EC research
Industrial & Engineering Chemistry Research
pubs.acs.org/IECR
Article

Single- and Multicomponent Fixed Bed Adsorption of CO_2, CH_4, and N_2 in Binder-Free Beads of 4A Zeolite

Lucas F. A. S. Zafanelli,* Adriano Henrique, Mohsen Karimi, Alírio E. Rodrigues, and José A. C. Silva*

Cite This: *Ind. Eng. Chem. Res.* 2020, 59, 13724−13734
Read Online

ACCESS | Metrics & More | Article Recommendations | Supporting Information

ABSTRACT: Single- and multicomponent adsorption fixed bed breakthrough experiments of carbon dioxide (CO_2), methane (CH_4), and nitrogen (N_2) on commercial binder-free beads of 4A zeolite have been studied at 313, 373, and 423 K and a total pressure of up to 5 bar. The ternary experiments ($CO_2/CH_4/N_2$) show a practically complete separation of CO_2 from CH_4/N_2 at all the temperatures studied, with selectivity at 313 K of CO_2 around 24 over CH_4 and 50 over N_2. The adsorption equilibrium data measured from the breakthrough experiments were modeled by the dual-site Langmuir isotherm, and the breakthrough results were simulated with a fixed bed adsorption model taking into account axial dispersion, mass-transfer resistances, and heat effects. The mathematical model predicts with a good accuracy the systematic behavior of the single- and multicomponent breakthrough results based on the independent parameters calculated from well-established correlations and intracrystalline diffusivities for zeolite 4A available in the literature. The results showed in the present work evidence that the binder-free beads of zeolite 4A can be employed to efficiently separate CO_2 from $CO_2/CH_4/N_2$ mixtures by fixed bed adsorption.

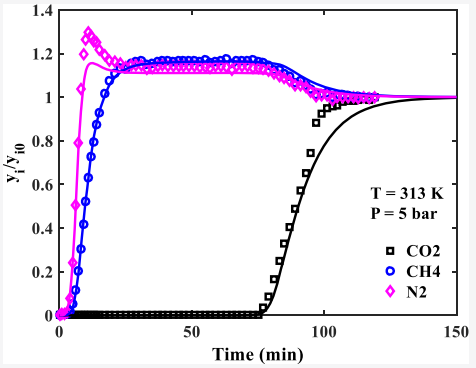

1. INTRODUCTION

Adsorption studies with mixtures containing CO_2, CH_4, and N_2 are important in several fields related to new renewable sources of energy.[1,2] Biogas is one example with a composition of CH_4 (50−70 vol %), CO_2 (30−40 vol %), and N_2 (0−10 vol %).[3,4] The presence of CO_2 in biogas reduces its calorific value, impairs its transport via pipelines, and, consequently, limits its use. Therefore, to use biogas as a vehicle fuel or to inject it into natural gas grids, it is important to remove (or to reduce to an acceptable specific value) CO_2. For instance, to inject biogas into natural gas grids, the CO_2 content must be lower than 3% (mol).[4]

Adsorption processes to separate CO_2 from the mixtures of $CO_2/CH_4/N_2$ are currently being used to upgrade biogas.[5,6] Conventional zeolites such as 13X, 5A, and 4A forms are known to have excellent properties to adsorb large amounts of CO_2, and at the same time, they have a significant selectivity (equilibrium or kinetic) relative to CH_4 and N_2.[7−14] To be used as adsorbents in industrial operations, they need to be transformed into pellets or beads as a bulk material made from the synthesized crystalline powder in order to avoid a high-pressure drop in cyclic adsorption processes. Conventional zeolite molecular sieve pellets/beads have a binder content of approximately 20%, which is in an inert form decreasing the adsorption capacity of the materials.[7,15] To overcome this issue, the so-called binder-free zeolite beads/pellets have been developed, where the binder is itself transformed into zeolite matter during hydrothermal conversion.[15] These binder-free zeolite beads or pellets have been studied systematically and have shown an increased adsorption capacity compared to the conventional binder-containing material.[5,7,8,11,15]

By far, the largest number of investigations have been devoted to study the single-component adsorption of CO_2, CH_4, and N_2 in zeolites and other materials.[9,11−14,16−19] Concerning zeolite 4A, some of them also reported the binary interaction adsorption between CH_4/N_2.[9,14,16] Ruthven and co-workers[12,13,20−22] among others[9−11,14,23] studied the single-component sorption kinetics of CO_2, CH_4, and N_2 in a wide range of size fractions of 4A zeolite crystals and commercial pellets by gravimetric and chromatographic methods. They showed that the ratio of intracrystalline diffusivities ($D_{c,i}/D_{c,j}$) is 15 for CO_2 over CH_4 and 20 for N_2 over CH_4 at 313 K.[12,13]

The well-known adsorption equilibrium hierarchy ($CO_2 \gg CH_4 > N_2$) in zeolite 4A, and the increase in the adsorption capacity of the so-called binder-free zeolite beads,[11] gives rise to an excellent sorption system to be exploited for the separation of these key compounds by fixed bed adsorption. Accordingly, the goal of this work is to evaluate the fixed bed adsorption dynamics of single and ternary mixtures of $CO_2/CH_4/N_2$ in this new type of binder-free beads of 4A zeolite, which is lacking in the

Received: April 15, 2020
Revised: June 30, 2020
Accepted: June 30, 2020
Published: June 30, 2020

Downloaded via INST POLITECNICO DE BRAGANCA 10900 on February 26, 2021 at 17:22:59 (UTC).
See https://pubs.acs.org/sharingguidelines for options on how to legitimately share published articles.

ACS Publications
© 2020 American Chemical Society

https://dx.doi.org/10.1021/acs.iecr.0c01911
Ind. Eng. Chem. Res. 2020, 59, 13724−13734

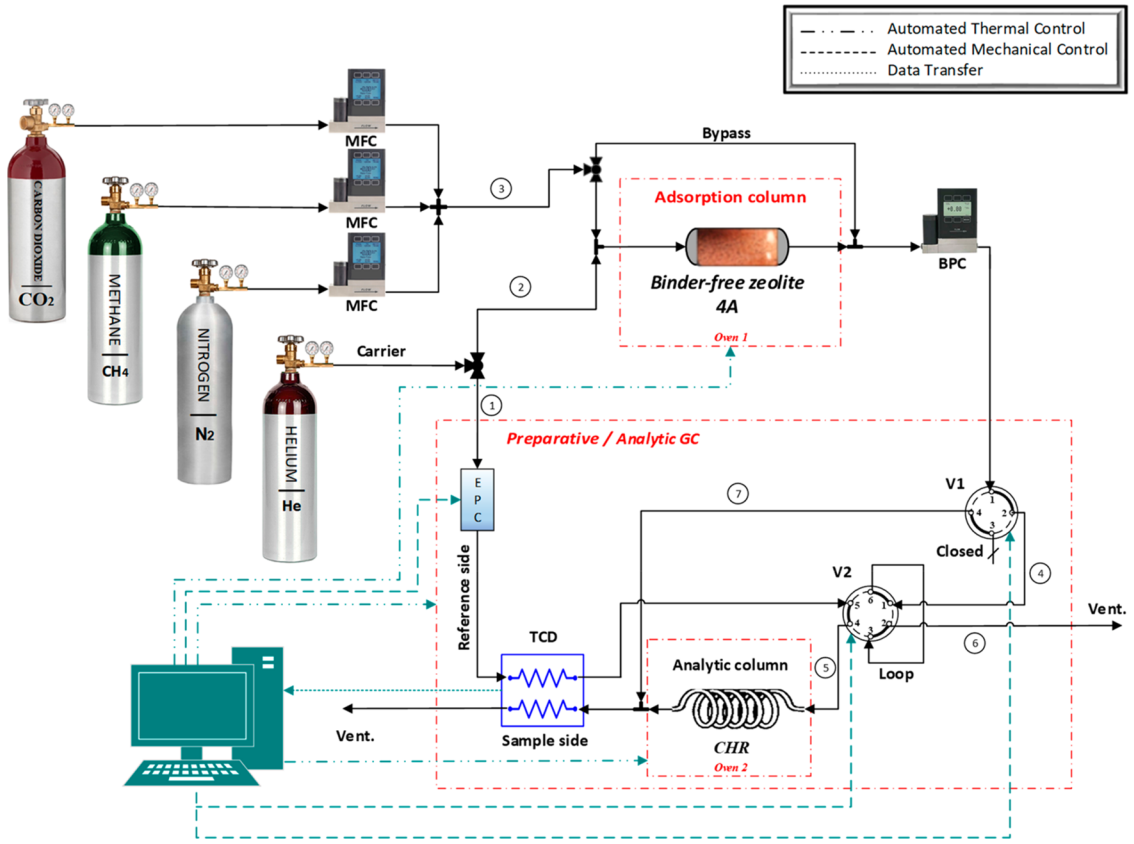

Figure 1. Schematic diagram of the experimental apparatus used to perform single- and multicomponent breakthrough experiments. MFC, mass flow controller; EPC, electric pressure controller; BPC, back-pressure controller; V1, four-way valve; V2, six-way valve; CHR, chromatographic silica gel column; and 1, 2, 3, 4, 5, 6, and 7, inside of circle, streams.

literature. For that, a series of single- and multicomponent breakthrough experiments were performed between 313 and 423 K and a total pressure of up to 5 bar. From the data, the adsorption equilibrium isotherms were collected. At the same time, a fixed bed adsorption dynamic mathematical model including the effect of (i) axial dispersion, (ii) mass-transfer resistances, and (iii) heat effects is developed to match the experiments and solved by the method of lines (MOL) in MATLAB code. The mathematical model parameters were determined independently from correlations available in the literature for zeolite 4A. The results arising from this work will be used in future work to study the cyclic separation of $CO_2/CH_4/N_2$ mixtures with interest for processes such as biogas upgrading by efficiently removing CO_2 from CH_4/N_2 using binder-free 4A zeolite beads.

2. EXPERIMENTAL SECTION

2.1. Binder-Free 4A Zeolite. The binder-free beads of zeolite 4A were supplied by Chemiewerk Bad Koestritz GmbH (Germany), which consist of spherical particles with a diameter size ranging from 1.6 to 2.5 mm made with zeolite 4A crystals with an average size of 1 μm. The synthesis and characterization are described in detail elsewhere.[11,24] In the Supporting Information (Table S1), a resume of the textural properties is given.

2.2. Breakthrough Apparatus. A single- and multicomponent breakthrough apparatus has been developed to study the fixed bed adsorption dynamics, which is presented in Figure 1. Briefly, the apparatus consists of three main sections: (i) a gas preparation section, (ii) an adsorption section, and (iii) an analytical section.

In the gas preparation section, the gas mixture ($CO_2/CH_4/N_2$) and inert helium (He) are mixed to be introduced into the system. He is used as a carrier gas and enters into the system from two streams: lines (1) and (2). Line (1) is sent directly to the reference side of the gas concentration detector (thermal conductivity detector, TCD), whereas line (2) is mixed with line (3) containing the adsorbable species. The mixture then passes through the adsorption column, which is placed in oven 1. The gas flow rate in line (1) is controlled by an electric pressure controller and the lines (2) and (3) by a mass flow controller.

This apparatus is designed to perform single- or multicomponent experiments, with the VICI Valco four-way valve (V1) being used to select the type of the experiment. In the adsorption section, the configuration shown in Figure 1 is selected to perform a multicomponent experiment (V1 in position A—solid lines). The pressure in the adsorption column is set up by a back-pressure controller, with the outlet flow being sent to port 1 of valve V1, which leaves by port 2. When the VICI Valco six-way valve (V2) is in position A, as shown in Figure 1, the flowing gas enters by port 1 [line (4)], passes by the loop, and leaves by port 2 directly to the vent through line (6). When valve V2 changes its position to B (dashed lines), the carrier gas exiting in the reference side of the TCD enters by port 4 and drags the sample contained within the loop to the capillary column in oven 2 through line (5) to analyze its composition at a predetermined time of the multicomponent breakthrough curve to be measured.

https://dx.doi.org/10.1021/acs.iecr.0c01911
Ind. Eng. Chem. Res. 2020, 59, 13724−13734

Table 1. Mathematical Model Equations for Fixed Bed Adsorption Simulation

phenomenon model	equations	
ideal gas	$C = \frac{P}{RT}$	(8)
overall mass balance	$\frac{\partial F}{\partial z} + \varepsilon_b \frac{\partial C}{\partial t} + \rho_p(1-\varepsilon_b)\sum_{i=1}^{n}\frac{\partial \bar{q}_i}{\partial t} = 0$	(9)
component mass balance	$-\varepsilon_b D_{ax}\frac{\partial}{\partial z}\left(C\frac{\partial y_i}{\partial z}\right) + \frac{\partial (F y_i)}{\partial z} + \varepsilon_b \frac{\partial (C y_i)}{\partial t} + \rho_p(1-\varepsilon_b)\frac{\partial \bar{q}_i}{\partial t} = 0$	(10)
mass-transfer rate	$\frac{\partial \bar{q}_i}{\partial t} = K_{LDF}(q^* - \bar{q}_i)$	(11)
Linear Driving Force (LDF)	$\frac{1}{K_{LDF}} = \frac{R_p}{3k_f} + \frac{{R_p}^2}{15\varepsilon_p D_p} + \frac{{r_c}^2}{15KD_c}$	(15)
gas-phase energy balance	$-K_{ax}\frac{\partial^2 T}{\partial z^2} + FC_{pg}\frac{\partial T}{\partial z} + C\varepsilon_b C_{pg}\frac{\partial T}{\partial t} + (1-\varepsilon_b)a_p h_p(T - T_s) + a_c h_w(T - T_w) = 0$	(12)
solid-phase energy balance	$\rho_p C_{ps}\frac{\partial T_s}{\partial t} = a_p h_p(T - T_s) + \rho_p\sum_{i=1}^{n}(-\Delta H_{st,i})\frac{\partial \bar{q}_i}{\partial t}$	(13)
isotherm model (DSL)	$q_i = \frac{q_{m1} b_{1i} p_i}{1 + \sum_{j=1}^{n} b_{1j} p_j} + \frac{q_{m2} b_{2i} p_i}{1 + \sum_{j=1}^{n} b_{2j} p_j}$	(7)

In the analytical section, line (5) goes to the chromatographic column (Supelco silica gel 3′′), with the effluent being detected in the sample side of the TCD.

To perform a single-component experiment, valve V1 must be in position B (dashed lines). In this situation, the output gas of the adsorption column enters by port 1 and leaves by port 4 (valve V1), bypassing valve V2 being directed to the sample side of the TCD through line (7). The dimension of the adsorption column (stainless steel) is 0.0286 m internal diameter and 0.0646 m length. For the experiments, the column contains 23.8 g (dry mass) of binder-free beads of zeolite 4A (BFK 1.6−2.5 mm), resulting in a bulk density of 590 kg m^{-3} in the bed. The textural properties of the binder-free beads of zeolite 4A (BFK 1.6−2.5 mm) have been reported elsewhere.[11] In the Supporting Information (Table S1), the characteristics of the adsorption column are resumed.

The adsorbates and inert gases were supplied by Air Liquide with the following purities: He ALPHAGAZ 2 (99.9998%), CO_2 N48 (99.998%), CH_4 N35 (99.95%), and nitrogen N50 (99.999%).

2.3. Experimental Procedure. Before the first run, the adsorption column is activated for 12 h at 623 K under vacuum and pure He flows (10 mL min^{-1}). This activating step under high temperature and vacuum is very important to remove the preadsorbed components, such as water, because the zeolites are highly hydrophilic.[12,15,25] After that, the gas in line (3) is mixed with He from line (2) to set up a partial pressure and enters the adsorption column to start the single- or multicomponent experiment. To perform a multicomponent experiment, valve 1 must be in position A (valve V1—solid lines), and for a single-component experiment, valve 1 must be in position B (valve V1—dashed lines). Thereafter, the experiment includes measuring the concentration of the gas at the outlet of the bed as a function of time by the TCD. The dynamic equilibrium loading is obtained by integrating the molar flow profiles of the breakthrough curves[26] by the following equation:

$$q_{exp,i} = \frac{1}{m_{ads}}\left(F_{f,i}t_n - \int_0^{t_\infty} F_i\, dt - \varepsilon_b V_c C_{i0}\right) \quad (1)$$

where m_{ads} is the adsorbent mass, $F_{f,i}$ is the feed molar flow rate of component i at the inlet of the bed, F_i is the molar flow rate of component i at the outlet of the bed, t_∞ is the saturation time, ε_b is the bed porosity, V_c is the column adsorption volume, and C_{0i} is the feed gas-phase concentration at the inlet of the fixed bed.

3. THEORETICAL CALCULATIONS

3.1. Adsorption Equilibrium Model. The dual-site Langmuir model (DSL) was used (eq 2) to predict the adsorption equilibria. In this model, the adsorbable species are distributed by two types of sites, each one following the Langmuir model assumption, with different binding energies and maximum adsorption capacity in each site[27,28]

$$q = q_{m1,i}\frac{b_{1i}p_i}{1 + b_{1i}p_i} + q_{m2,i}\frac{b_{2i}p_i}{1 + b_{2i}p_i} \quad (2)$$

where $q_{m1,i}$ and $q_{m2,i}$ are the maximum adsorbed concentrations of component i in each site and b_{1i} and b_{2i} are the adsorption affinity constants of component i in each site. This model deviates from the ideal Langmuir model accounting for certain heterogeneity of adsorbent surface. It reverts to the Langmuir model if we consider only one site.

The effect of temperature on the adsorption affinity constant, b_i, is taken into account by the integrated van't Hoff equation

$$b_i = b_{\infty,i}e^{(-\Delta H_i/RT)} \quad (3)$$

where $b_{\infty,i}$ is the pre-exponential factor of the affinity constant at an infinite temperature, R is the ideal gas constant, $-\Delta H_i$ is the heat of adsorption, and T is the temperature.

The heat of adsorption as a function of the amount adsorbed is the so-called isosteric heat[29] defined by

https://dx.doi.org/10.1021/acs.iecr.0c01911
Ind. Eng. Chem. Res. 2020, 59, 13724−13734

$$\frac{\Delta H_{st}}{RT^2} = -\left(\frac{\partial \ln p}{\partial T}\right)_q \quad (4)$$

Considering ΔH_{st} independent of temperature, this relationship can be used to evaluate it by integrating eq 4 directly at a fixed coverage from the experimentally measured adsorption isotherms in a plot of ln p against $1/T$[30]

$$\ln p = \text{constant} - \frac{\Delta H_{st}}{RT} \quad (5)$$

The study of isosteric heat as a function of loading can put in evidence materials with heterogeneous behavior.[25,27] It is commonly accepted that the isosteric heat of sorption of CO_2 on zeolites A, X, and Y decreases with coverage.[29] This behavior can be predicted by the differentiation of the DSL model (eq 2), assuming constant loading ($dq = 0$), and substituting the result in the isosteric heat equation (eq 4), resulting in the following equation:[27,31]

$$(-\Delta H_{st}) = \frac{q_{m1}\frac{b_1\Delta H_1}{(1+b_1p)^2} + q_{m2}\frac{b_2\Delta H_2}{(1+b_2p)^2}}{q_{m1}\frac{b_1}{(1+b_1p)^2} + q_{m2}\frac{b_2}{(1+b_2p)^2}} \quad (6)$$

Equation 6 can predict the increase or decrease of the isosteric heat with loading depending on the heterogeneity of the adsorbent. In the limit, the value can be constant if the surface is homogeneous when the adsorption occurs in identical homogeneous sites (Langmuir equation).

The extended DSL model isotherm to multicomponent systems is given by the following equation:

$$q_i = q_{m1,i}\frac{b_{1i}p_i}{1+\sum_{j=1}^{n} b_{1j}p_j} + q_{m2,i}\frac{b_{2i}p_i}{1+\sum_{j=1}^{n} b_{2j}p_j} \quad (7)$$

3.2. Mathematical Modeling of Single- and Multicomponent Fixed Bed Breakthrough Curves. The dynamic behavior of the adsorption process can be numerically predicted according to the mass and energy conservation laws. We use a mathematical model that includes both the effect of axial dispersion and mass-transfer resistances taking into account by an overall effective rate mass-transfer coefficient, which is an extension of the Glueckauf linear rate driving force model (LDF).[30,32] The adsorption equilibrium is described by a thermodynamic model calibrated from the breakthrough experimental data measured in this work.

Consequently, the mathematical model developed to simulate the transient behavior of single and gas mixture of $CO_2/CH_4/N_2$ results in a set of coupled partial and algebraic differential equations (PDAEs) summarized in Table 1.

3.3. Numerical Solution of Model Equations. For the solution of the model, the set of coupled PDAEs are reduced into a system of ordinary and algebraic differential equations (ODAEs) by applying the MOL.[33] The MOL is classified as a simple discretization or a semidiscrete method because only the space coordinate is discretized, whereas the time is kept continuous. The spatial coordinate was discretized by orthogonal collocation (OC). The computation of the collocation points was determined by the position on the spatial coordinate using the Jacobi polynomial, $P_N^{(\alpha,\beta)}(x)$. The approximation of the first and second derivatives was made by collocation matrix routines $A_{i,j}$ and $B_{i,j}$, respectively. In the Villadsen and Michelsen's book, detailed information about the OC method, as well as several subroutines to solve the PDE equations, is available.[34]

In the present work, the collocation points were given by the zeros of Jacobi polynomials $P_N^{(\alpha,\beta)}(x)$, with $\alpha = 0$ and $\beta = 0$. The resulting system of ODAEs was integrated using a high-order stiff integrator, ode15s, available in the MATLAB library.[35] Twenty-five collocation points appeared to give satisfactory accuracy and stability to the solution.

4. RESULTS AND DISCUSSION

4.1. Single-Component Adsorption. The single-component adsorption equilibrium data of CO_2, CH_4, and N_2 were collected at three temperatures, 313, 373, 423 K, and for partial pressures up to 3.5 bar directly from the fixed bed breakthrough experiments using eq 1.[5,7,8,36] Helium was used as an inert gas (to set up a broader range of partial pressures of adsorbates), with the experimental conditions being reported in Table S4 in the Supporting Information. Figure 2a−c shows the measured experimental breakthrough curves (symbols) plotted in terms of normalized molar fraction y_i/y_{i0} as a function of moles fed per unit mass of the adsorbent at 313 K for the three components by the order of their decreasing affinity: (a) CO_2, (b) CH_4, and (c) N_2 (the data measured at 373 and 423 K are shown in the Supporting Information, Figures S1−S3). Figure 2 clearly shows that the moles fed to reach the breakthrough of CO_2 (Figure 2a) are much more than those in the case of CH_4 (Figure 2b) and N_2 (Figure 2c). It is also clear in each figure that as the partial pressure increases, the moles fed to reach the breakthrough also increase, which indicates that the data are thermodynamically consistent. The breakthrough hierarchy order and therefore the affinity is $CO_2 \gg CH_4 > N_2$.

From the breakthrough data shown in Figures 2a−c and S1−S3 in the Supporting Information, the adsorption equilibrium data were collected by applying eq 1. Figure 3a shows the isotherms measured for CO_2 (symbols) and the fitting with the DSL model (lines). CO_2 is strongly adsorbed especially at 313 K, with the isotherm being typically of type I (and highly nonlinear), which also explains the sharp nature of the breakthrough profiles of CO_2 observed in Figure 2a that practically approach a constant pattern form. Regarding the fitting of the DSL model shown in Figure 3a, the model describes the equilibrium data with good accuracy.

Figure 3b,c shows the isotherms measured for CH_4 and N_2 (symbols), respectively, and the respective fitting with the Langmuir model (lines) (only one site was used in eq 2 to fit the data reasonably). This is so because the isotherms approach practically a linear form in the range of partial pressures and temperatures studied, giving rise to a much lower affinity to the adsorbent, and consequently, the breakthrough profiles (Figure 2b,c) are less sharp than those in the case of CO_2 because dispersive forces overcome the strong effect of the highly favorable nature of the isotherm in the shape of the concentration profiles, as can be seen in the case of CO_2 (Figures 2a and 3a).[9,11,14] The amount adsorbed at 313 K and partial pressure 3.5 bar is significantly different between the compounds, which is around 4.48, 1.35, and 0.81 mol kg_{ads}^{-1} for CO_2, CH_4, and N_2, respectively, which is comparable with other values reported in the literature.[11,37] As an example, the loadings of CO_2 on this new binder-free zeolite 4A are practically 26% higher than the ones measured by Ahn et al.[10] in an inert pelletized form and 7% lower than the ones measured by Yucel and Ruthven[13] in a pure powder form. These comparisons point out that the commercial binder-free zeolite studied in this work

https://dx.doi.org/10.1021/acs.iecr.0c01911
Ind. Eng. Chem. Res. 2020, 59, 13724−13734

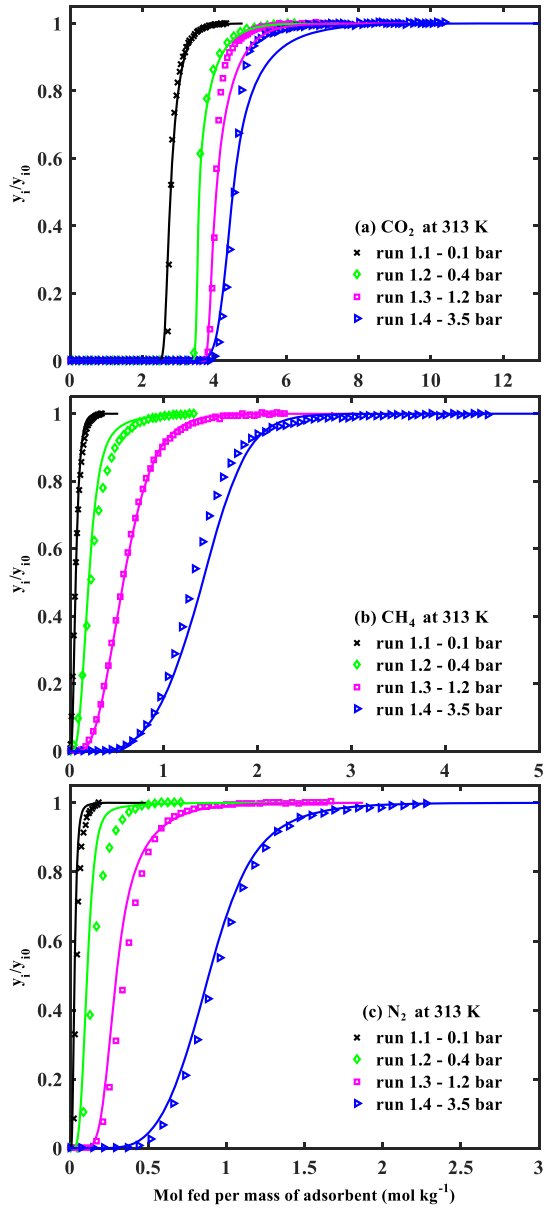

Figure 2. Experimental (symbols) and numerical (lines) breakthrough curves of CO_2 (a), CH_4 (b), and N_2 (c) on binder-free 4A zeolite at 313 K.

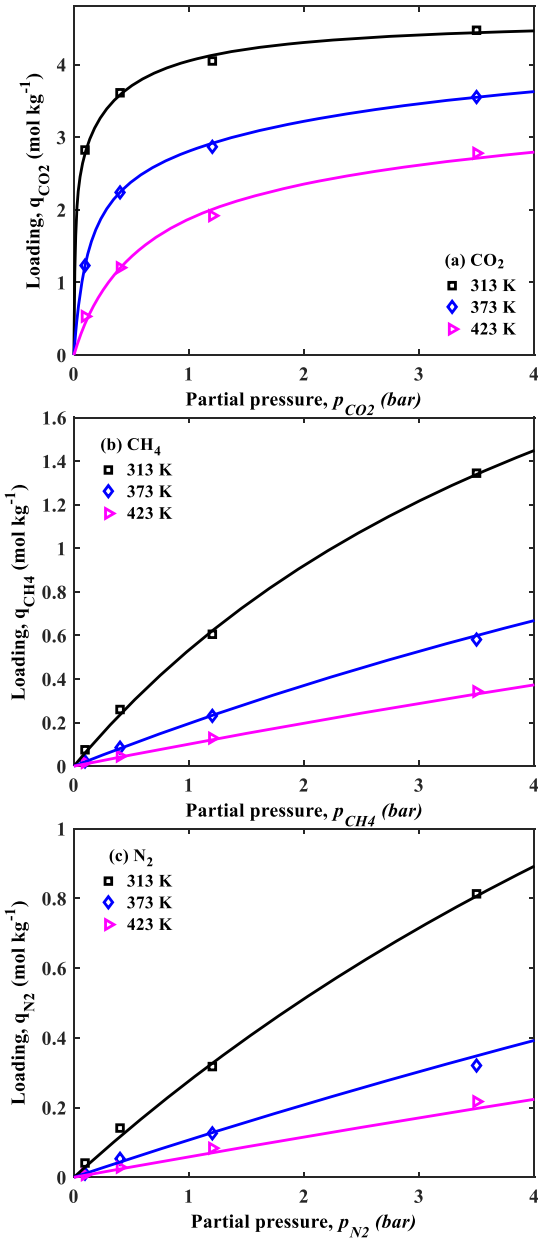

Figure 3. Adsorption equilibrium isotherms of CO_2 (a), CH_4 (b), and N_2 (c) in binder-free 4A zeolite. Solid lines represent the isotherm model predictions and symbols the experimental data.

indeed increases its adsorption working capacity. Table 2 summarizes the parameters for the best fit of the DSL and Langmuir isotherms for the adsorption of CO_2, CH_4, and N_2 in the binder-free zeolite 4A.

The isosteric heat of adsorption for CO_2, CH_4, and N_2 as a function of the amount adsorbed was also calculated from the experimental data by applying eq 5 and numerically through eq 6.[27] Figure 4 shows the experimental and numerical isosteric heat as a function of coverage for CO_2, CH_4, and N_2, where it can be seen that the DSL model predicts the experimental observation of the slight decrease of the net isosteric heat of CO_2 as a function of coverage. This behavior has already been observed for CO_2 in zeolites A, X, and Y and can be explained by the charge density in such zeolites that interact with the strong quadrupole moment of the CO_2 molecule, giving rise to a heterogeneous surface.[29] For the Langmuir model and assuming that the maximum adsorbed concentration is temperature-independent, the isosteric heat (lines) must be constant, as can be seen in Figure 4 for CH_4 and N_2.

Table 2. Adsorption Equilibrium Model Parameters for Sorption of CO_2, CH_4, and N_2 on Binder-Free 4A Zeolite

	Q_m (mol kg^{-1})		b (bar^{-1})[a]		(ΔH_i) (kJ mol^{-1})	
species	q_{m1}	q_{m2}	b_1	b_2	$(\Delta H_i)_1$	$(\Delta H_i)_2$
CO_2	1.97	2.68	2.44	88.3	−35.6	−38.7
CH_4	3.39		0.19		−18.0	
N_2	3.47		0.09		−16.2	

[a]The reference temperature used is 313.15 K.

4.2. Multicomponent Adsorption of $CO_2/CH_4/N_2$ Mixtures. The breakthrough experiments for $CO_2/CH_4/N_2$ mixtures were performed according to the procedure described in Section 2. Figure 5a–c shows the experimental breakthrough

https://dx.doi.org/10.1021/acs.iecr.0c01911
Ind. Eng. Chem. Res. 2020, 59, 13724−13734

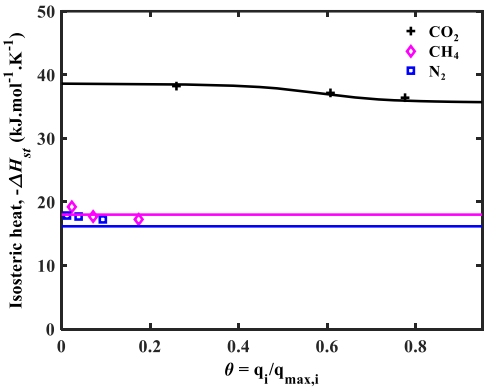

Figure 4. Experimental (symbols) and predicted (lines) isosteric heat of sorption of CO_2, CH_4, and N_2 against fractional loading. The experimental values were calculated by applying eq 5 and numerical values through eq 6.

curves (symbols) for the temperatures 313 (a), 373 (b), and 423 K (c), respectively, plotted in terms of normalized molar fraction y_i/y_{i0} against time for a total pressure of 5 bar. Table S5 (Supporting Information) summarizes the experimental conditions for the ternary mixture. As shown in Figure 5, CO_2 is the most adsorbed component, and CH_4 and N_2 breakthrough practically together just at the beginning of the experiments. This effect is observed at all the temperatures studied, being an excellent result where CO_2 is practically completely separated from CH_4/N_2.

4.3. Modeling of Single- and Multicomponent Breakthrough Curves. Mathematical modeling provides a robust tool for the design of adsorption separation units to study the best operating conditions, as well as to test the thermodynamic and kinetic parameters, for later use in the design of cyclic adsorption processes. Therefore, the single- and multicomponent breakthrough curves were matched with the mathematical model described in Section 3.2 (Table 1) taking into account (i) contributions of axial dispersion, (ii) mass-transfer resistances through a linear driving force (LDF) rate model, and (iii) heat effects in the bed. Because both axial dispersion and mass-transfer resistances cause zone spreading,[38] a careful analysis should be made to calculate the proper parameters of the model.

Before the simulations, and as a first approach, the relative importance of the individual axial dispersion and mass-transfer resistances can be evaluated from the method of moments for a linear system by an overall effective rate coefficient k' (eq 14),[30] which includes both the effects of axial dispersion and mass-transfer resistances for a biporous adsorbent such as the binder-free 4A zeolite.[30] This relationship is a generalization of the Glueckauf approximation by comparison of the moments for the simple linear rate plug flow model and the general diffusion model with axial dispersion, being an easier way to evaluate the dominant mass-transfer mechanism in the system.[30]

$$\frac{1}{k'K} = \frac{D_{ax}}{v_i^2}\left(\frac{1-\varepsilon_b}{\varepsilon_b}\right) + \frac{R_p}{3k_f} + \frac{R_p^2}{15\varepsilon_p D_p} + \frac{r_c^2}{15KD_c} \qquad (14)$$

where k' is the overall effective rate coefficient (s^{-1}), K is the dimensionless Henry's law equilibrium constant (-), D_{ax} is the axial dispersion ($m^2\ s^{-1}$), v_i is the interstitial velocity ($m\ s^{-1}$), ε_b is the bed porosity (-), R_p is the particle radius (m), ε_p is the particle porosity (-), D_p is the effective macropore diffusivity ($m^2\ s^{-1}$), r_c is the crystal radius (m), and D_c is the intracrystalline diffusivity ($m^2\ s^{-1}$).

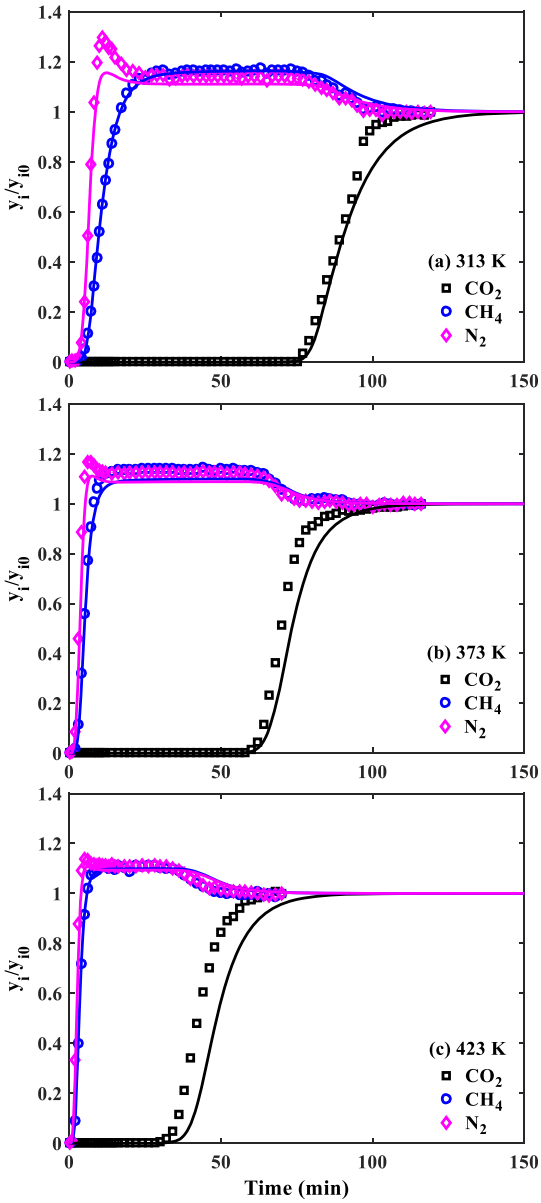

Figure 5. Experimental (symbols) and numerical (lines) breakthrough curves for the ternary mixture of $CO_2/CH_4/N_2$ on binder-free zeolite 4A at 313 (a), 373 (b), and 423 K (c) and 5 bar pressure.

Moreover, for the mathematical model presented in Section 3.2, the last three terms of eq 14 represent the LDF overall rate coefficient, (K_{LDF}), as follows:

$$\frac{1}{K_{LDF}} = \frac{R_p}{3k_f} + \frac{R_p^2}{15\varepsilon_p D_p} + \frac{r_c^2}{15KD_c} \qquad (15)$$

Malek and Farooq[39] further generalize eq 15 for nonlinear systems by setting the adsorption equilibrium parameter K (dimensionless Henry's law coefficient of the isotherm or slope of the isotherm outside the validity of Henry's law) equal to the ratio between the adsorbed phase concentration in equilibrium with the feed concentration, $K = \rho_p q_{0f}/C_{0f}$, for an initial clean bed as a simplification to estimate K_{LDF} for studies in nonlinear systems.

https://dx.doi.org/10.1021/acs.iecr.0c01911
Ind. Eng. Chem. Res. 2020, 59, 13724−13734

Table 3. Calculated Values of Each Term of the rhs of eq 14 and lhs of eq 15 for the Single-Component Experimental Runs Performed with CO_2, CH_4, and N_2 in Binder-Free Zeolite 4A at 313 K[a]

run	$\frac{D_{ax}}{v_i^2}\left(\frac{1-\varepsilon_b}{\varepsilon_b}\right)$ [b] (s)	$\frac{R_p}{3k_f}$ [b] (s)	$\frac{R_p^2}{15\varepsilon_p D_p}$ [b] (s)	$\frac{r_c^2}{15KD_c}$ [b] (s)	$\frac{1}{K_{LDF}}$ [c] (s)
			CO_2		
1.1	1.84	3.10×10^{-3}	9.63×10^{-3}	2.17×10^{-5}	1.27×10^{-2}
1.2	1.83	3.06×10^{-3}	9.63×10^{-3}		1.27×10^{-2}
1.3	5.61	9.17×10^{-3}	2.11×10^{-2}		3.02×10^{-2}
1.4	9.25	1.52×10^{-2}	3.25×10^{-2}		4.77×10^{-2}
			CH_4		
1.1	2.06	2.68×10^{-3}	7.28×10^{-3}	1.22×10^{-1}	1.32×10^{-1}
1.2	2.04	2.66×10^{-3}	7.28×10^{-3}		1.32×10^{-1}
1.3	6.29	7.98×10^{-3}	1.71×10^{-2}		1.47×10^{-1}
1.4	10.22	1.32×10^{-2}	2.69×10^{-2}		1.63×10^{-1}
			N_2		
1.1	2.15	2.60×10^{-3}	7.88×10^{-3}	1.28×10^{-2}	2.33×10^{-2}
1.2	2.16	2.57×10^{-3}	7.88×10^{-3}		2.33×10^{-2}
1.3	6.49	7.72×10^{-3}	1.74×10^{-2}		3.79×10^{-2}
1.4	10.92	1.28×10^{-2}	2.69×10^{-2}		5.25×10^{-2}

[a]At 373 and 423 K, the values are reported in the Supporting Information (Table S6). [b]The correlations used to estimate the parameters in this table are found in the Supporting Information (Table S2). [c]The value of this term is the sum of the three mass-transfer terms according to eq 15.

Table 4. Calculated Values of Each Term of the rhs of eq 14 and lhs of eq 15 for the Multicomponent Ternary Experimental Runs $CO_2/CH_4/N_2$ on Binder-Free Zeolite 4A

run	T (K)	specie	$\frac{D_{ax}}{v_i^2}\left(\frac{1-\varepsilon_b}{\varepsilon_b}\right)$ [a] (s)	$\frac{R_p}{3k_f}$ [a] (s)	$\frac{R_p^2}{15\varepsilon_p D_p}$ [a] (s)	$\frac{r_c^2}{15KD_c}$ [a] (s)	$\frac{1}{K_{LDF}}$ [b] (s)
M1	313	CO_2	1.98	1.45×10^{-2}	6.26×10^{-2}	2.17×10^{-5}	7.71×10^{-2}
		CH_4	2.23	1.26×10^{-2}	5.24×10^{-2}	1.22×10^{-1}	1.87×10^{-1}
		N_2	2.21	1.22×10^{-2}	5.40×10^{-2}	1.28×10^{-2}	7.90×10^{-2}
M2	373	CO_2	2.50	1.10×10^{-2}	4.66×10^{-2}	4.79×10^{-5}	5.77×10^{-2}
		CH_4	2.86	9.55×10^{-3}	3.87×10^{-2}	7.09×10^{-2}	1.19×10^{-1}
		N_2	2.78	9.31×10^{-3}	4.05×10^{-2}	6.83×10^{-3}	5.67×10^{-2}
M3	423	CO_2	2.78	9.02×10^{-3}	3.84×10^{-2}	7.65×10^{-5}	4.74×10^{-2}
		CH_4	3.18	7.86×10^{-3}	3.18×10^{-2}	4.97×10^{-2}	8.94×10^{-2}
		N_2	3.08	7.64×10^{-3}	3.37×10^{-2}	4.55×10^{-3}	4.59×10^{-2}

[a]The correlations used to estimate the parameters in this table are found in the Supporting Information (Table S2). [b]The value of this term is the sum of the three mass-transfer terms according to eq 15.

For the evaluation of each term of eq 14, the parameters D_{ax}, k_f, and D_p were estimated from correlations reported in the literature (see the Supporting Information, Table S2).[11−13,30] For the intracrystalline diffusivity, we use the values reported by Yucel and Ruthven,[12,13] which are shown in Table S3 of the Supporting Information. These values were calculated from uptake rate experiments in a wide size fraction of pure zeolite 4A crystals (7.3−34 μm).

Table 3 summarizes the corresponding values of each term shown in eq 14 for the single-component experiments performed at 313 K. At 373 and 423 K, the values are shown in the Supporting Information (Table S6).

As can be seen in Table 3 for the single-component experiments, the first term of the rhs of eq 14, which quantifies the effect of axial mass dispersion in the bed, is much higher than all the other terms. For instance, in the case of CO_2 and N_2, the axial dispersion term is at least 100 times higher than the film, macropore, and micropore time constants. This difference is smaller in the case of CH_4, with the axial dispersion term being at least 20 times higher. The same behavior is observed at 373 and 423 K (Table S6). This is also valid for the multicomponent experiments as can be seen in Table 4. Accordingly, Tables 3, 4, and S6 clearly show that zone spreading in the fixed bed adsorption system under study is influenced only by the axial mass dispersion. This is demonstrated, in the Supporting Information, with a parametric study using the mathematical model (Table 1) to see the effect of changing the model parameters [axial dispersion (D_{ax}) or overall mass-transfer coefficient (K_{LDF})] in the computed concentration profiles of CO_2, CH_4, and N_2. As expected, Figures S4−S6 in the Supporting Information clearly show that the concentration profile is sensitive to the axial mass dispersion (D_{ax}) because of the small changes in its value, causing significant changes in the concentration−response profile, whereas this effect is not seen when the value of the overall mass-transfer coefficient (K_{LDF}) changes. It is well known that both dispersion and mass transfer cause zone spreading, and sometimes it is difficult to evaluate which mechanism is the dominant one.[30,38,40] Tables 3, 4, and

https://dx.doi.org/10.1021/acs.iecr.0c01911
Ind. Eng. Chem. Res. 2020, 59, 13724−13734

Table 5. Calculated Model Parameters for the Simulation of Single-Component Breakthrough Experiments at 313 K[a]

run	K_{LDF}[b] (s^{-1})	D_{ax}[b] ($m^2\ s^{-1}$)	K_{ax}[b] ($W\ m^{-1}\ K^{-1}$)	C_{pg}[b] ($J\ mol^{-1}\ K^{-1}$)	h_p[b] ($W\ m^{-2}\ K^{-1}$)	h_w ($W\ m^{-2}\ K^{-1}$)
			CO_2			
1.1	78.5	1.76×10^{-4}	0.31	2.78	167	29.3
1.2	78.7	1.77×10^{-4}	0.18	1.39	92	29.9
1.3	33.1	5.84×10^{-5}	0.18	1.37	90	44.5
1.4	21	1.47×10^{-5}	0.15	1.02	52	58
			CH_4			
1.1	7.56	1.85×10^{-4}	0.24	4.24	175	29.6
1.2	7.56	1.86×10^{-4}	0.20	3.04	109	24.0
1.3	6.78	6.14×10^{-5}	0.20	3.10	113	27.8
1.4	6.15	3.72×10^{-5}	0.17	2.56	74	27.9
			N_2			
1.1	42.9	1.86×10^{-4}	0.25	4.13	181	23.6
1.2	43.0	1.86×10^{-4}	0.20	2.75	117	26.2
1.3	26.4	6.20×10^{-5}	0.20	1.78	110	52.4
1.4	19.1	3.71×10^{-5}	0.16	1.27	67	57.8

[a]At 373 and 423 K, the parameters are given in the Supporting Information (Table S7). [b]The correlations used to estimate the parameters in this table are found in the Supporting Information (Table S2).

Table 6. Calculated Model Parameters for the Simulation of Ternary Breakthrough Experiments

	K_{LDF}[a] (s^{-1})			D_{ax}[a] ($m^2\ s^{-1}$)						
run	CO_2	CH_4	N_2	CO_2	CH_4	N_2	K_{ax}[a] ($W\ m^{-1}\ K^{-1}$)	C_{pg}[a] ($J\ mol^{-1}\ K^{-1}$)	h_p[a] ($W\ m^{-2}\ K^{-1}$)	h_w ($W\ m^{-2}\ K^{-1}$)
M1	13.0	5.3	12.7	1.50×10^{-5}	1.72×10^{-5}	1.70×10^{-5}	0.20	1.02	50	123
M2	17.3	8.4	17.7	3.29×10^{-6}	2.29×10^{-5}	2.23×10^{-5}	0.22	1.09	57	108
M3	21.1	11.2	21.8	3.97×10^{-6}	1.85×10^{-5}	1.78×10^{-5}	0.22	1.16	63	102

[a]The correlations used to estimate the parameters in this table are found in the Supporting Information (Table S2).

S6 and Figures S4−S6 prove that for the present system, the axial dispersion mechanism dominates the zone spreading in the bed.

Accordingly, all the simulations of the single- and multicomponent experiments were conducted by using parameters for the axial dispersion and overall mass-transfer coefficient K_{LDF} taken from correlations and intracrystalline diffusivities reported in the literature with the values shown in Tables 5, 6, and S7. The lines represented in Figures 2a−c, 5a−c, and S1−S3 in the Supporting Information show the simulated results for all the single- and multicomponent runs, where we can see a reasonable agreement with the experimental data.

Also regarding the values reported in Table 3, it should be noted that to decrease the effect of axial dispersion in zone spreading, the interstitial velocity needed to be 30 times higher, which is a value impossible to set up in our experimental system (and probably many others). The previous observations can also explain some discrepancies between the reported kinetic data (intracrystalline diffusivities) for $CO_2/CH_4/N_2$ measured in zeolite 4A and other materials by neglecting the important effect of axial dispersion in the measurement of mass-transfer resistances in fixed bed adsorption studies (pulse or frontal chromatography).[11−13]

Figure 5 also shows that the binder-free 4A zeolite is an excellent adsorbent to separate CO_2 from a ternary mixture $CO_2/CH_4/N_2$. The separation efficiency of the binder-free zeolite 4A beads was evaluated in terms of the equilibrium sorption selectivity defined by $S_{i,j} = (q_i/y_i)/(q_j/y_j)$, where q is the loading of the adsorbed component and y is the molar fraction of the component in the gas phase. The equilibrium selectivity was calculated from the equilibrium data reported in Table 2. The selectivities at 313 K and 5 bar are $S_{CO_2/CH_4} = 24$, $S_{CO_2/N_2} = 50$, and $S_{CH_4/N_2} = 2$, where the values are similar to other values reported in the literature.[9,41−44]

5. CONCLUSIONS

In this work, single- and multicomponent studies of CO_2, CH_4, and N_2 adsorption on binder-free beads of 4A zeolite have been investigated through a series of fixed bed breakthrough adsorption experiments at 313, 373, and 423 K and a total pressure of up to 5 bar. The calculated amounts adsorbed at 313 K and partial pressure 3.5 bar are around 4.48, 1.35, and 0.81 mol kg_{ads}^{-1} for CO_2, CH_4, and N_2, respectively. The CH_4 and N_2 adsorption isotherms were fitted with the Langmuir isotherm and CO_2 with the DSL isotherm. The experimental isosteric heat of CO_2 decreases slightly with loading, with this effect being predicted with the DSL model. The multicomponent breakthrough data show practically a complete separation between CO_2 and CH_4/N_2. The simulated data show that the dynamics of the fixed bed adsorption system studied in this work are dominated by zone spreading because of axial dispersion with no contribution from mass-transfer resistances. In general, the mathematical model shown in this work predicts the single- and multicomponent experiments of CO_2, CH_4, and N_2 on binder-free zeolite 4A beads with good accuracy, with all parameters calculated independently from the correlations and intracrystalline diffusivities taken from the literature, being a valuable tool for the design of cyclic adsorption processes (pressure swing adsorption, thermal swing adsorption, or electric swing adsorption). Finally, the present work shows that the commercial binder-free beads of zeolite 4A act as an efficient separator of CO_2 from CH_4/N_2 with selectivity around 24 over CH_4 and 50 over N_2, being a good alternative to be used in

https://dx.doi.org/10.1021/acs.iecr.0c01911
Ind. Eng. Chem. Res. 2020, 59, 13724−13734

industrial operations for the removal of CO_2 from $CO_2/CH_4/N_2$ mixtures (e.g., biogas upgrading).

■ ASSOCIATED CONTENT

Supporting Information

The Supporting Information is available free of charge at https://pubs.acs.org/doi/10.1021/acs.iecr.0c01911.

Textural properties of the adsorbent and adsorption column; correlations for estimating mathematical model parameters and intracrystalline diffusivities; experimental conditions and model parameters for all the experiments and breakthrough curves at 373 and 423 K; and parametric study effect of the influence of axial dispersion and mass-transfer resistances on breakthrough curves with the mathematical model (PDF)

■ AUTHOR INFORMATION

Corresponding Authors

Lucas F. A. S. Zafanelli − *Centro de Investigação de Montanha (CIMO), Instituto Politécnico de Bragança, Campus de Santa Apolónia, 5300-253 Bragança, Portugal;* orcid.org/0000-0001-5187-2042; Phone: +351 924 073 500; Email: zafanelli@ipb.pt

José A. C. Silva − *Centro de Investigação de Montanha (CIMO), Instituto Politécnico de Bragança, Campus de Santa Apolónia, 5300-253 Bragança, Portugal;* orcid.org/0000-0003-1778-3833; Phone: +351 273 30 3125; Email: jsilva@ipb.pt

Authors

Adriano Henrique − *Centro de Investigação de Montanha (CIMO), Instituto Politécnico de Bragança, Campus de Santa Apolónia, 5300-253 Bragança, Portugal; Laboratory of Separation and Reaction Engineering (LSRE), Associate Laboratory LSRE/LCM, Department of Chemical Engineering, Faculty of Engineering, University of Porto, 4099-002 Porto, Portugal;* orcid.org/0000-0002-5227-9790

Mohsen Karimi − *Centro de Investigação de Montanha (CIMO), Instituto Politécnico de Bragança, Campus de Santa Apolónia, 5300-253 Bragança, Portugal; Laboratory of Separation and Reaction Engineering (LSRE), Associate Laboratory LSRE/LCM, Department of Chemical Engineering, Faculty of Engineering, University of Porto, 4099-002 Porto, Portugal;* orcid.org/0000-0002-1886-5454

Alírio E. Rodrigues − *Laboratory of Separation and Reaction Engineering (LSRE), Associate Laboratory LSRE/LCM, Department of Chemical Engineering, Faculty of Engineering, University of Porto, 4099-002 Porto, Portugal;* orcid.org/0000-0002-0715-4761

Complete contact information is available at: https://pubs.acs.org/10.1021/acs.iecr.0c01911

Funding

The authors would like to acknowledge (i) Kristin Gleichmann and Chemiewerk Bad Koestritz GmbH for kindly providing the binder-free beads of zeolite 4A studied in this work and (ii) the comments and suggestions of the anonymous reviewer of this paper that help us to improve significantly the contents and analysis of the results. The authors acknowledge the financial support from (1) Project "VALORCOMP" (ref.0119_VALORCOMP_2_P), financed through INTERREG V A Spain Portugal (POCTEP) 2014−2020, under the European Regional Development Fund by FCT; (2) Project POCI-01-0145-FEDER006984-Associate Laboratory LSRE-LCM funded by ERDF through COMPETE2020, Programa Operacional Competitividade e Internacionalização (POCI), and by national funds through FCT—Fundação para a Ciência e a Tecnologia; (3) Foundation for Science and Technology (FCT, Portugal) and ERDF under Programme PT2020 to CIMO (UID/AGR/00690/2019); (4) National funding by FCT, Foundation for Science and Technology, through the individual research grant SFRH/BD/140550/2018 of Mohsen Karimi; (5) National funding by FCT, Foundation for Science and Technology, through the individual research grant SFRH/BD/148525/2019 of Adriano Henrique; and (6) The authors are grateful to the Foundation for Science and Technology (FCT, Portugal) for financial support by national funds FCT/MCTES to CIMO (UIDB/00690/2020).

Notes

The authors declare no competing financial interest.

■ NOMENCLATURE

a_p	specific area of the pellet (m^{-1})
a_c	specific area of the column (m^{-1})
b_i	adsorption equilibrium constant of component i (bar^{-1})
$b_{\infty,i}$	frequency factor of component i (bar^{-1})
C	total gas concentration (mol m^{-3})
C_f	feed gas concentration (mol m^{-3})
C_{pg}	heat capacity of gas (J mol^{-1} K^{-1})
C_{ps}	heat capacity of solid (J g^{-1} K^{-1})
d_b	beads diameter (m)
d_c	column diameter (m)
D_{ax}	axial mass dispersion coefficient (m^2 s^{-1})
D_m	molecular diffusivity (m^2 s^{-1})
D_p	effective macropore diffusivity (m^2 s^{-1})
D_k	Knudsen diffusivity (m^2 s^{-1})
D_c	intracrystalline diffusivity (m^2 s^{-1})
F	total molar flux (mol m^{-2} s^{-1})
h_p	film heat-transfer coefficient (W m^{-2} K^{-1})
h_w	wall heat-transfer coefficient (W m^{-2} K^{-1})
K_{LDF}	linear driving force coefficient (s^{-1})
K_{ax}	effective axial bed thermal conductivity (W m^{-1} K^{-1})
K	dimensionless Henry's law equilibrium constant (-)
k'	overall effective rate coefficient (s^{-1})
k_f	film mass-transfer coefficient (m s^{-1})
L	length of column (m)
M_i	molecular mass of component i (kg $kmol^{-1}$)
m_{ads}	mass of adsorbent (kg)
p_i	partial pressure of component i (bar)
P	total pressure of column (bar)
P_{em}	Peclet number (-)
q_i	adsorbed phase concentration of component i (mol kg^{-1})
$\overline{q}_i$	average adsorbed phase concentration of component i (mol kg^{-1})
q^*	equilibrium adsorbed concentration of component (mol kg^{-1})
q_m	maximum adsorbed phase concentration (mol kg^{-1})
r_c	crystal radius (m)
R_p	particle radius (m)
R	universal gas constant (J mol^{-1} K^{-1})
S_{ij}	selectivity of component i over j (-)
t	time (s)
T	temperature in bulk gas phase (K)
T_s	temperature in solid phase (K)
T_w	column wall temperature (K)

https://dx.doi.org/10.1021/acs.iecr.0c01911
Ind. Eng. Chem. Res. 2020, 59, 13724−13734

v_i interstitial velocity (m s^{-1})
y_i molar fraction of component i (-)
z axial coordinate in bed (m)

GREEK LETTERS

ΔH_i heat adsorption of species i (J mol^{-1})
ΔH_{st} isosteric heat adsorption (J mol^{-1})
ε_b bed porosity
ε_p particle porosity
ρ_p apparent density (kg m^{-3})
ρ_s solid density (kg m^{-3})
θ $=q/q_m$

REFERENCES

(1) Canevesi, R. L. S.; Andreassen, K. A.; Da Silva, E. A.; Borba, C. E.; Grande, C. A. Pressure Swing Adsorption for Biogas Upgrading with Carbon Molecular Sieve. *Ind. Eng. Chem. Res.* **2018**, *57*, 8057−8067.
(2) Santos, M. P. S.; Grande, C. A.; Rodrigues, A. E. Pressure Swing Adsorption for Biogas Upgrading. Effect of Recycling Streams in Pressure Swing Adsorption Design. *Ind. Eng. Chem. Res.* **2011**, *50*, 974−985.
(3) Yousef, A. M. I.; Eldrainy, Y. A.; El-Maghlany, W. M.; Attia, A. Upgrading Biogas by a Low-Temperature CO_2 Removal Technique. *Alexandria Eng. J.* **2016**, *55*, 1143−1150.
(4) Sun, Q.; Li, H.; Yan, J.; Liu, L.; Yu, Z.; Yu, X. Selection of Appropriate Biogas Upgrading Technology-a Review of Biogas Cleaning, Upgrading and Utilisation. *Renewable Sustainable Energy Rev.* **2015**, *51*, 521−532.
(5) Silva, J. A. C.; Schumann, K.; Rodrigues, A. E. Sorption and Kinetics of CO_2 and CH_4 in Binderless Beads of 13X Zeolite. *Microporous Mesoporous Mater.* **2012**, *158*, 219−228.
(6) Choi, S.; Drese, J. H.; Jones, C. W. Adsorbent Materials for Carbon Dioxide Capture from Large Anthropogenic Point Sources. *ChemSusChem* **2009**, *2*, 796−854.
(7) Silva, J. A. C.; Ferreira, A.; Mendes, P. A. P.; Cunha, A. F.; Gleichmann, K.; Rodrigues, A. E. Adsorption Equilibrium and Dynamics of Fixed Bed Adsorption of CH_4/N_2 in Binderless Beads of 5A Zeolite. *Ind. Eng. Chem. Res.* **2015**, *54*, 6390−6399.
(8) Silva, J. A. C.; Cunha, A. F.; Schumann, K.; Rodrigues, A. E. Binary Adsorption of CO_2/CH_4 in Binderless Beads of 13X Zeolite. *Microporous Mesoporous Mater.* **2014**, *187*, 100−107.
(9) Mohr, R. J.; Vorkapic, D.; Rao, M. B.; Sircar, S. Pure and Binary Gas Adsorption Equilibria and Kinetics of Methane and Nitrogen on 4A Zeolite by Isotope Exchange Technique. *Adsorption* **1999**, *5*, 145−158.
(10) Ahn, H.; Moon, J.-H.; Hyun, S.-H.; Lee, C.-H. Diffusion Mechanism of Carbon Dioxide in Zeolite 4A and CaX Pellets. *Adsorption* **2004**, *10*, 111−128.
(11) Seabra, R.; Ribeiro, A. M.; Gleichmann, K.; Ferreira, A. F. P.; Rodrigues, A. E. Adsorption Equilibrium and Kinetics of Carbon Dioxide, Methane and Nitrogen on Binderless Zeolite 4A Adsorbents. *Microporous Mesoporous Mater.* **2019**, *277*, 105−114.
(12) Yucel, H.; Ruthven, D. M. Diffusion in 4A Zeolite. *J. Chem. Soc., Faraday Trans. 1* **1980**, *76*, 60−70.
(13) Yucel, H.; Ruthven, D. M. Diffusion of CO_2 in 4A and 5A Zeolite Crystals. *J. Colloid Interface Sci.* **1980**, *74*, 186−195.
(14) Habgood, H. W. The Kinetics of Molecular Sieve Action. Sorption of Nitrogen−Methane Mixtures By Linde Molecular Sieve 4a. *Can. J. Chem.* **1958**, *36*, 1384−1397.
(15) Gleichmann, K.; Unger, B.; Brandt, A. *Industrial Zeolite Molecular Sieves*; Intech, 2016; Vol. *i*, p 13.
(16) Ruthven, D. M.; Kumar, R. A Chromatographic Study of the Diffusion of N_2, CH_4 and Binary CH_4-N_2 Mixtures in 4A Molecular Sieve. *Can. J. Chem. Eng.* **1979**, *57*, 342−348.
(17) Perez-Carbajo, J.; Matito-Martos, I.; Balestra, S. R. G.; Tsampas, M. N.; Van De Sanden, M. C. M.; Delgado, J. A.; Águeda, V. I.; Merkling, P. J.; Calero, S. Zeolites for CO_2-CO-O_2 Separation to Obtain CO_2-Neutral Fuels. *ACS Appl. Mater. Interfaces* **2018**, *10*, 20512−20520.
(18) Couck, S.; Lefevere, J.; Mullens, S.; Protasova, L.; Meynen, V.; Desmet, G.; Baron, G. V.; Denayer, J. F. M. CO_2, CH_4 and N_2 Separation with a 3DFD-Printed ZSM-5 Monolith. *Chem. Eng. J.* **2017**, *308*, 719−726.
(19) Morales-Ospino, R.; Santiago, R. G.; Siqueira, R. M.; de Azevedo, D. C. S.; Bastos-Neto, M. Assessment of CO_2 Desorption from 13X Zeolite for a Prospective TSA Process. *Adsorption* **2020**, *26*, 813−824.
(20) Haq, N.; Ruthven, D. M. A Chromatographic Study of Sorption and Diffusion in 5A Zeolite. *J. Colloid Interface Sci.* **1986**, *112*, 164−169.
(21) Ruthven, D. M. Sorption of Oxygen, Nitrogen, Carbon Monoxide, Methane, and Binary Mixtures of These Gases in 5A Molecular Sieve. *AIChE J.* **1976**, *22*, 753−759.
(22) Ruthven, D. M. Short Communication: Diffusion of Simple Molecules in 4A Zeolite. *Adsorption* **2001**, *7*, 301−304.
(23) Ward, J. W.; Habgood, H. W. The Infrared Spectra of Carbon Dioxide Adsorbed on Zeolite X. *J. Phys. Chem.* **1966**, *70*, 1178−1182.
(24) Pavlov, M. L.; Travkina, O. S.; Kutepov, B. I. Grained Binder-Free Zeolites: Synthesis and Properties. *Catal. Ind.* **2012**, *4*, 11−18.
(25) Sircar, S.; Myers, A. Gas Separation by Zeolites. In *Handbook of Zeolite Science and Technology*; Auerbach, S., Carrado, K., Dutta, P., Eds.; Marcel Dekker Inc.: New York, 2003; pp 1063−1116.
(26) Henrique, A.; Rodrigues, A. E.; Silva, J. A. C. Separation of Hexane Isomers in ZIF-8 by Fixed Bed Adsorption. *Ind. Eng. Chem. Res.* **2019**, *58*, 378−394.
(27) Do, D. D. *Adsorption Analysis: Equilibria and Kinetics*; World Scientific, 1998; Vol. *2*.
(28) Foo, K. Y.; Hameed, B. H. Insights into the Modeling of Adsorption Isotherm Systems. *Chem. Eng. J.* **2010**, *156*, 2−10.
(29) Barrer, R. M. *Zeolites and Clay Minerals as Sorbents and Molecular Sieves, VII*; Academic Press: London, 1978.
(30) Ruthven, D. M. *Principles of Adsorption and Adsorption Processes*, 1st ed.; John Wiley & Sons: New York, 1984.
(31) Bárcia, P. S.; Nicolau, M. P. M.; Gallegos, J. M.; Chen, B.; Rodrigues, A. E.; Silva, J. A. C. Modeling Adsorption Equilibria of Xylene Isomers in a Microporous Metal-Organic Framework. *Microporous Mesoporous Mater.* **2012**, *155*, 220−226.
(32) Glueckauf, E. Theory of Chromatography. *Trans. Faraday Soc.* **1955**, *51*, 34−44.
(33) Schiesser, W. E.; Griffiths, G. W. *A Compendium of Partial Differential Equation Models: Method of Lines Analysis with Matlab Installation of Matlab Files Running an Application*; Cambridge University Press: Cambridge, 2009.
(34) Villadsen, J.; Michelsen, M. L. *Solution of Differential Equation Models by Polynomial Approximation*; Prentice-Hall, 1978.
(35) Shampine, L. F.; Reichelt, M. W. The MATLAB ODE Suite. *SIAM J. Sci. Comput.* **1997**, *18*, 1−22.
(36) Bastin, L.; Bárcia, P. S.; Hurtado, E. J.; Silva, J. A. C.; Rodrigues, A. E.; Chen, B. A Microporous Metal-Organic Framework for Separation of CO_2/N_2 and CO_2/CH_4 by Fixed-Bed Adsorption. *J. Phys. Chem. C* **2008**, *112*, 1575−1581.
(37) Eagan, J. D.; Anderson, R. B. Kinetics and Equilibrium of Adsorption on 4A Zeolite. *J. Colloid Interface Sci.* **1975**, *50*, 419−433.
(38) Wankat, P. C. *Rate-Controlled Separations*; Blackie Academic & Professional: London, 1990.
(39) Malek, A.; Farooq, S. Kinetics of Hydrocarbon Adsorption on Activated Carbon and Silica Gel. *AIChE J.* **1997**, *43*, 761−776.
(40) Lapidus, L.; Amundson, N. R. Mathematics of Adsorption in Beds. Vi. The Effect of Longitudinal Diffusion in Ion Exchange and Chromatographic Columns'. *J. Phys. Chem.* **1952**, *56*, 984−988.
(41) Akten, E. D.; Siriwardane, R.; Sholl, D. S. Monte Carlo Simulation of Single- and Binary-Component Adsorption of CO_2, N_2, and H_2 in Zeolite Na-4A. *Energy Fuels* **2003**, *17*, 977−983.
(42) Himeno, S.; Tomita, T.; Suzuki, K.; Yoshida, S. Characterization and Selectivity for Methane and Carbon Dioxide Adsorption on the All-Silica DD3R Zeolite. *Microporous Mesoporous Mater.* **2007**, *98*, 62−69.
(43) Delgado, J. A.; Uguina, M. A.; Gómez, J. M.; Ortega, L. Adsorption Equilibrium of Carbon Dioxide, Methane and Nitrogen

https://dx.doi.org/10.1021/acs.iecr.0c01911
Ind. Eng. Chem. Res. 2020, 59, 13724−13734

onto Na- and H-Mordenite at High Pressures. *Sep. Purif. Technol.* **2006**, *48*, 223−228.
(44) Palomino, M.; Corma, A.; Jordá, J. L.; Rey, F.; Valencia, S. Zeolite Rho: A Highly Selective Adsorbent for CO_2/CH_4 Separation Induced by a Structural Phase Modification. *Chem. Commun.* **2012**, *48*, 215−217.

https://dx.doi.org/10.1021/acs.iecr.0c01911
Ind. Eng. Chem. Res. 2020, 59, 13724−13734